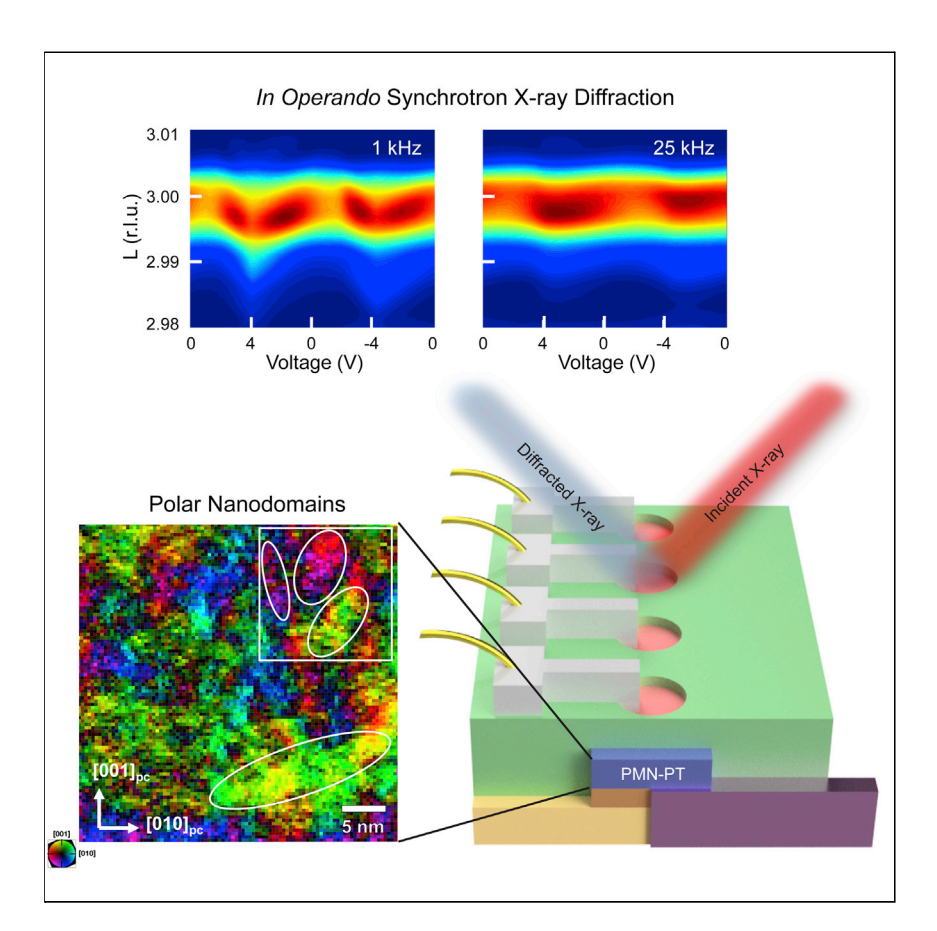
**Matter** 



### **Article**

# Frequency-dependent suppression of fieldinduced polarization rotation in relaxor ferroelectric thin films



We report a comprehensive study of polarization rotation dynamics in thin films of the prototypical relaxor ferroelectric 0.68PbMg $_{1/3}$ Nb $_{2/3}$ O $_3$ -0.32PbTiO $_3$ . The combination of *in operando* X-ray diffraction, scanning transmission electron microscopy, and switching dynamics studies reveals the frequency-dependent behavior of polarization evolution and rotation.

Jieun Kim, Derek J. Meyers, Abinash Kumar, ..., James M. LeBeau, Philip J. Ryan, Lane W. Martin

jieun.kim@berkeley.edu (J.K.) lwmartin@berkeley.edu (L.W.M.)

#### Highlights

*In operando* X-ray diffraction of polarization rotation

Observation of polar nanodomains by scanning transmission electron microscopy

Suppression of polarization rotation by polar nanodomains at high frequency



Kim et al., Matter 4, 2367–2377 July 7, 2021 © 2021 Elsevier Inc. https://doi.org/10.1016/j.matt.2021.04.017



# **Matter**



#### **Article**

# Frequency-dependent suppression of field-induced polarization rotation in relaxor ferroelectric thin films

Jieun Kim,<sup>1,\*</sup> Derek J. Meyers,<sup>1,2</sup> Abinash Kumar,<sup>3</sup> Abel Fernandez,<sup>1</sup> Gabriel A.P. Velarde,<sup>1</sup> Zishen Tian,<sup>1</sup> Jong-Woo Kim,<sup>4</sup> James M. LeBeau,<sup>3</sup> Philip J. Ryan,<sup>4</sup> and Lane W. Martin<sup>1,5,6,\*</sup>

#### **SUMMARY**

The dynamics of polarization evolution and rotation in 0.68PbMg<sub>1/3</sub> Nb<sub>2/3</sub>O<sub>3</sub>-0.32PbTiO<sub>3</sub> relaxor ferroelectric thin films are studied via in operando synchrotron-based X-ray diffraction with AC electric fields. A frequency-limited suppression of polarization rotation was observed above ultrasonic frequencies ( $\gtrsim 20$  kHz). The nature of this suppression is informed by scanning transmission electron microscopy in the zero-field state, where a high density of nanoscale, low-angle domain walls was observed. In combination with switching dynamics studies, the results suggest that the suppression of polarization rotation at ultrasonic frequencies is due to the large activation field needed to move the domain walls when the polarization rotates between different monoclinic phases. These results are critical in understanding piezoelectric relaxation phenomena in relaxor ferroelectrics.

#### INTRODUCTION

Relaxor ferroelectrics (relaxors) have attracted intense research efforts in the last few decades due to their large dielectric and piezoelectric properties. When an electric field is applied along the non-polar [001] to domain-engineered single-crystal relaxors, extremely high values of the piezoelectric constant ( $d_{33}$ ) can be achieved. These large effects are generally explained via a polarization rotation mechanism. Theoretical studies have shown that the motion of atoms within the unit cell follows a minimum energy pathway to reach thermodynamic equilibrium under electric fields. This pathway was confirmed in neutron and X-ray diffraction studies, which reported field-induced phase transitions. Although such atomicand macroscopic-scale pictures provide a compelling mechanism for the large effects, the role of mesoscopic-scale polar entities (e.g., polar nanodomains, PNDs), 5,6 which could account for as much as 50%–80% of the total dielectric and piezoelectric properties, is not fully understood. In particular, recent theoretical studies suggested that domain walls may facilitate polarization rotation, contributing to the large electromechanical coupling in domain-engineered relaxor single crystals.

To elucidate these mesoscale contributions to the large field-driven effects, field-induced phase transitions should be examined dynamically, since the contributions from mesoscale entities exhibit strong relaxation and thus can be effectively quenched at high frequency. Previous studies, however, have been performed mostly under thermodynamic equilibrium conditions, for example, by using DC electric fields or poled samples. <sup>4,7,9</sup> As a result, the role of PNDs in accommodating field-induced phase transitions during the application of AC electric fields remains poorly

#### **Progress and potential**

The giant electromechanical coupling in relaxor ferroelectrics originates from field-induced polarization rotation. To gain a comprehensive picture of the mechanism by which polarization rotation occurs, understanding the basic thermodynamics and dynamics of polarization rotation is crucial. Although thermodynamic stabilities of different phases along the polarization rotation path are relatively well understood, little is known about their dynamics. Here, we use in operando X-ray diffraction with AC electric fields to study the dynamics of phase evolution during polarization rotation in thin films of the prototypical relaxor ferroelectric 0.68PbMg<sub>1/3</sub>Nb<sub>2/3</sub>O<sub>3</sub>-0.32PbTiO<sub>3</sub>. We observe that polarization rotation is suppressed at high frequencies due to the coupling between unit cells and mesoscopic domains. Our results provide a better understanding of the complex nature of field-induced polarization rotation in relaxor ferroelectrics.







understood.<sup>10</sup> This gap in understanding originates not only from the complex nature of relaxors, which involve competition between various forces that occur over large length and time scales, <sup>11,12</sup> but also from experimental challenges in directly observing the dynamic aspects of field-induced phase transitions during operation. Recent advances in AC electric field-dependent diffraction (e.g., at beamline 6-ID-B at the Advanced Photon Source) provide opportunities to probe *in operando* field-induced structural response in relaxor thin films.

Here, it is shown that the field-induced phase transitions are strongly dependent on AC electric field frequency even though the magnitude of the switched polarization remains the same. Polarization rotation is suppressed at ultrasonic frequencies (≥ 20 kHz), consistent with previous measurements of piezoelectric strain using interferometry techniques, 13 and is roughly 2 orders of magnitude slower than the frequency at which non-180° domain-wall motion becomes suppressed in ferroelectrics (~1–10 MHz). <sup>14</sup> Scanning transmission electron microscopy (STEM) studies suggest that the difference in the timescale of suppression of domain-wall motion could arise from the mesoscale domain structure, which consists of a very high density of nanometer-sized domains separated by low-angle domain walls. Switching dynamics studies show that the activation field for domain-wall motion deviates from lower frequency values at ultrasonic frequencies, which suggests that the atomicscale polarization rotation is limited by the timescale of mesoscale domain switching. Thus, we propose that the suppression of polarization rotation at ultrasonic frequencies is due to the coupling of polarization rotation to domain switching, which occurs at much slower timescales due to the high density of low-angle domain walls in relaxor ferroelectrics. 12,15,16

#### **RESULTS**

#### Measurement setup for in operando synchrotron-based X-ray microdiffraction

Heterostructures of 100 nm SrRuO<sub>3</sub> (SRO, top electrode)/50 nm 0.68PbMg<sub>1/3</sub>Nb<sub>2/3</sub>  $O_3$ -0.32PbTi $O_3$  (PMN-PT)/25 nm  $Ba_{0.5}Sr_{0.5}RuO_3$  (BSRO, bottom electrode)/NdSc $O_3$ (110) were synthesized via pulsed-laser deposition using established procedures (experimental procedures). Previously, we performed detailed structural studies of PMN-PT grown on several substrates to study the effect of epitaxial strain. 15 It was found that for films grown on  $NdScO_3$  substrates, corresponding to -0.5% compressive strain, the PMN-PT exhibits butterfly-shaped diffuse-scattering patterns, which are a structural signature of PMN-PT on the PMN-rich side with rhombohedral-like macroscopic symmetry. <sup>17</sup> To enable the *in operando* measurements, a microfabrication process was applied to produce device structures that allow for microdiffraction to be performed directly on the capacitor under applied AC fields; details of the device fabrication process are provided (experimental procedures and Figure S1). A schematic of the final measurement setup (Figure 1A) and a micrograph of the actual device (Figure 1B) are provided. To complete the measurements, X-rays with a photon energy of 10 keV were passed through a pinhole with a diameter of  $25 \mu m$ . The X-rays were aligned with the active device by mapping the sample surface at a diffraction condition for the platinum contact pads (experimental procedures). A gated point detector (avalanche photodiode) synchronized with the voltage source was used to collect the diffracted intensities as a function of voltage as the AC voltage was cycled across the capacitor. This allows for the collection of diffracted intensities in real time as the voltage is swept at different frequencies. At each measurement step, intensities were collected for 30 s (e.g., corresponding to  $3 \times 10^5$  cycles for measurements at 10 kHz) to ensure sufficient counting statistics at each bin (experimental procedures and Figure S2). For the switching dynamics studies,

<sup>&</sup>lt;sup>1</sup>Department of Materials Science and Engineering, University of California, Berkeley, Berkeley, CA 94720, USA

<sup>&</sup>lt;sup>2</sup>Department of Physics, Oklahoma State University, Stillwater, OK 74078, USA

<sup>&</sup>lt;sup>3</sup>Department of Materials Science and Engineering, Massachusetts Institute of Technology, Cambridge, MA 02139, USA

<sup>&</sup>lt;sup>4</sup>Advanced Photon Source, Argonne National Laboratory, Argonne, IL 60439, USA

<sup>&</sup>lt;sup>5</sup>Materials Sciences Division, Lawrence Berkeley National Laboratory, Berkeley, CA 94720, USA

<sup>&</sup>lt;sup>6</sup>Lead contact

<sup>\*</sup>Correspondence: jieun.kim@berkeley.edu (J.K.), lwmartin@berkeley.edu (L.W.M.)

https://doi.org/10.1016/j.matt.2021.04.017





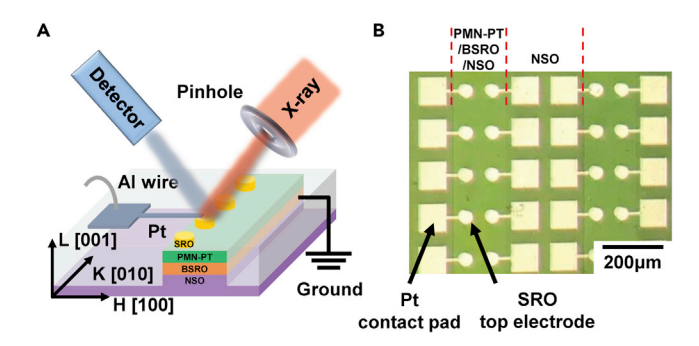


Figure 1. Experimental setup of *in operando* X-ray diffraction with AC electric field (A) Schematic of measurement setup. NSO, NdScO<sub>3</sub>. (B) Optical microscope image of actual device.

polarization hysteresis loop measurements were performed using a ferroelectric tester (Radiant Technologies) at the same frequency range as the *in operando* diffraction experiments.

#### Suppressed polarization rotation above ultrasonic frequencies

Voltage- and frequency-dependent in operando X-ray diffraction experiments were performed about the PMN-PT 003-diffraction condition. All scans were performed by incrementally increasing in L from (H, K, L) = (0, 0, 2.98) to (0, 0, 3.01). At each L position, the voltage was cycled with a given frequency, while the intensities were collected at steps of 0.25 V (50 kV/cm) to a maximum voltage of  $\pm 4$  V (or  $\pm 800$  kV/cm), a value sufficient to saturate the switched polarization in the frequency range 0.1-100 kHz. Representative raw data at 1 (Figure 2A), 10 (Figure 2B), and 25 kHz (Figure 2C) are shown as 2D maps in which the vertical and horizontal axes correspond to the reciprocal lattice vector L of the PMN-PT and the voltage, respectively. Data at 0.1 kHz (50, 75, 100 kHz) are similar to the data at 1 kHz (25 kHz), as are the data for positive and negative voltages; thus, for brevity, only a subset of the data is shown here, but all data are provided elsewhere (Figures S3-S6). At all frequencies, the peaks shift to lower L with increasing voltage due to the elongation of the lattice along the [001] under applied voltage (Figures 2D-2F). Qualitative differences are observed between the data for 1 kHz and the higher frequencies ( $\geq$  10 kHz). At 1 kHz, two sharp diffraction peaks are observed near 2.996 reciprocal lattice units (rlu) (Figure 2A,1 rlu  $\equiv$  1/4.05 Å), whereas only one broad peak is observed at the L for higher frequencies (arrows, Figures 2A-2C). Furthermore, the intensity profile is quite diffuse at 4 V due to the appearance of another peak around 2.99 rlu (blue curves, Figures 2D and 2E), which suggests increased structural disorder due to a field-induced phase transition from a higher- to a lower-symmetry phase with larger lattice parameter.

To probe the field-induced phase transition in more detail, X-ray diffraction profiles were fitted using a Voigt function (i.e., a convolution of Gaussian and Lorentzian profiles)  $^{18}$  (Figures 2D–2F) to extract the phase fractions as a function of voltage and frequency (Figures 2G–2I). The fitting results for all frequencies (0.1 to 25 kHz) and voltages (–4 to 4 V) are provided (Figures S7–S15). In the following, we use the monoclinic notations  $M_{\rm A}$  and  $M_{\rm C}$  following Vanderbilt and Cohen.  $^{19}$  For zero field, we model the PMN-PT films as a mixture of rhombohedral (R) and monoclinic ( $M_{\rm A}$ ) phases based on the observation of butterfly-shaped diffuse-scattering patterns and  $M_{\rm A}$ -type splitting  $^{20}$  in reciprocal space mapping about the PMN-PT 103-diffraction condition (Figure S16). Further support for R and  $M_{\rm A}$  coexistence is provided by STEM analysis of oxygen octahedral distortion patterns wherein checkerboard and





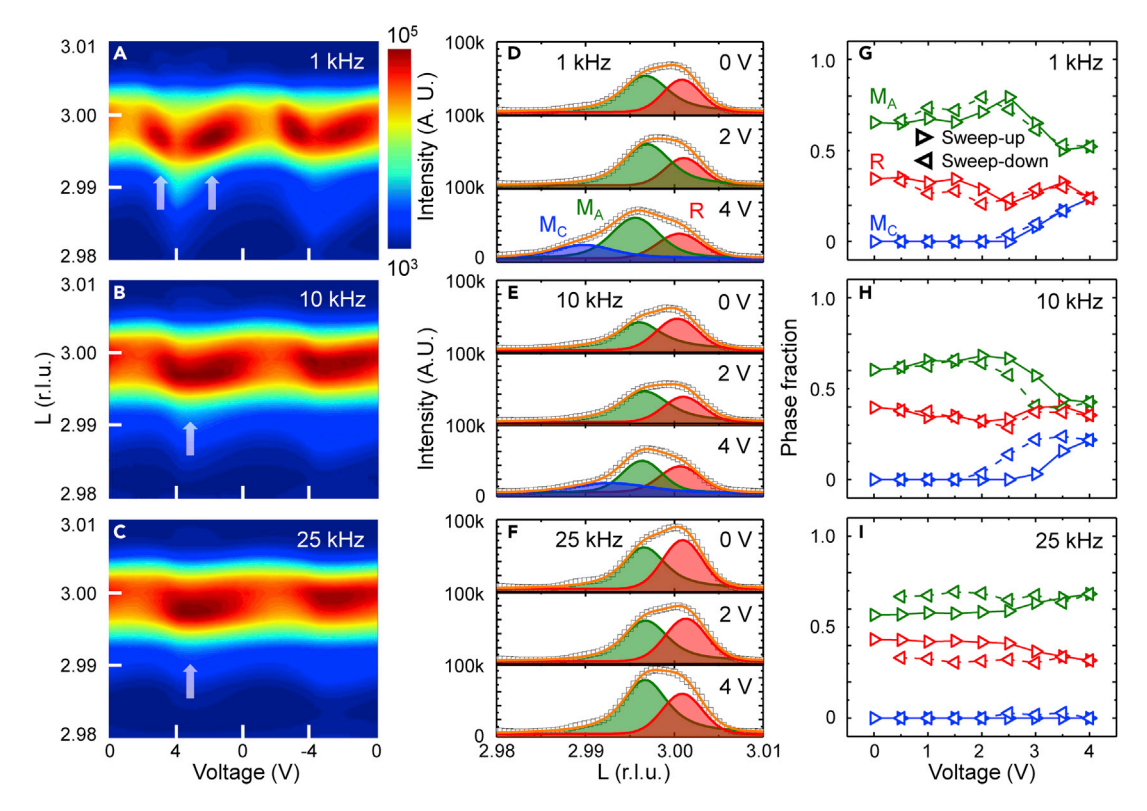


Figure 2. In operando X-ray diffraction of PMN-PT about the PMN-PT 003-diffraction condition

(A–C) Reciprocal lattice vector L versus voltage at (A) 1 kHz, (B) 10 kHz, and (C) 25 kHz. The white arrows indicate the peak diffracted intensities.

(D–F) Intensity versus reciprocal lattice vector L for different voltages at (D) 1 kHz, (E) 10 kHz, and (F) 25 kHz. Empty squares represent data points for diffracted intensities and the orange lines represent the sum of the fitted curves. Individual fitting curves are shown as curves with filled colors for comparison of integrated areas with red, green, and blue representing the R, M<sub>A</sub>, and M<sub>C</sub> phases, respectively.

(G–I) Phase fraction versus voltage at (G) 1 kHz, (H) 10 kHz, and (I) 25 kHz.

stripe patterns indicate R- and monoclinic-like distortions, respectively (Figure S17).  $^{16}$  With increasing electric field, the  $M_A$  phase can be reversibly transformed to the M<sub>C</sub> phase.<sup>4</sup> Therefore, we fitted the X-ray diffraction profiles assuming the phase coexistence of either R and MA or R, MA, and MC, taking whichever gives the best fitting results at each voltage. At zero voltage, the X-ray diffraction profile is broad for all frequencies, and fits reveal a mixture of R (red) and MA (green) phases (Figures 2D-2F). Upon increasing the voltage to 2 V for all frequencies, the X-ray diffraction profiles reveal an increased fraction of the MA phase (resulting from polarization rotation and transformation of R to M<sub>A</sub>), as can be seen by the increased intensity and larger-area green curve (Figures 2D-2F). By further increasing the voltage to 4 V, the emergence of a third peak—centered at 2.99 rlu—corresponding to the  $M_C$  (blue) phase is observed at 1 and 10 kHz (Figures 2D and 2E). At 25 kHz, however, there is almost no change in intensity at 2.99 rlu, but only a further increase in the intensity at 2.996 rlu, corresponding to the MA phase (Figure 2F), thus indicating that the MA-to-MC phase transition is limited at this frequency. A summary of the evolution of the phase fraction of the R, MA, and MC phases as a function of voltage for all frequencies is provided (Figures 2G-2I). At both 1 and 10 kHz, the phase fractions reveal that at 4 V the PMN-PT is the most inhomogeneous, even though the average lattice parameter is the largest, thus favoring M<sub>C</sub> (Figures 2G and 2H). The increased inhomogeneity, which can be seen in increasing fractions of R and M<sub>C</sub> and decreasing fractions of M<sub>A</sub>, indicates that the energy barrier between R, MA, and MC is lower under an electric field, which is consistent with the



observation of supercritical states in PMN-PT.<sup>21</sup> During the sweep-down of the voltage, data at 1 kHz show that the recovery of the MA phase is fully reversible and, correspondingly, the M<sub>C</sub> phase completely disappears (Figure 2G). This is consistent with observations of stable MA phase upon removal of electric field and reversible M<sub>A</sub>-to-M<sub>C</sub> phase transitions in DC electric-field measurements.<sup>4</sup> Examination of the data at 10 and 25 kHz, however, reveals differences from DC electric-field measurements (Figures 2H and 2I). At 10 kHz, the M<sub>A</sub>-to-M<sub>C</sub> phase transition shows hysteresis between the sweep-up and the sweep-down of voltage. The hysteresis at 10 kHz suggests that the dynamics of the  $M_A$ -to- $M_C$  phase transition are on the order of such a timescale (0.1 ms). On the other hand, almost no  $M_A$ -to- $M_C$  phase transition is observed in the entire voltage range at 25 kHz and above, suggesting a frequencylimited suppression of the M<sub>A</sub>-to-M<sub>C</sub> transition (Figure 2I). The R-to-M<sub>A</sub> transition is still observed at 25 kHz, which indicates that polarization rotation within a single monoclinic (M<sub>A</sub>) plane occurs at a timescale faster than the M<sub>A</sub>-to-M<sub>C</sub> transition, which involves a discontinuous jump of polarization, known as the c-axis jump, between two monoclinic ( $M_A$  and  $M_C$ ) planes.<sup>22</sup>

#### **Observation of domain structures**

To elucidate the origin of frequency-limited suppression of the  $M_A$ -to- $M_C$  phase transition, high-resolution high-angle annular dark field (HAADF) STEM imaging was performed on a PMN-PT thin-film sample in the zero-field state (Figure 3A). As expected, the epitaxial nature of the PMN-PT and BSRO (bottom electrode) films on the NdScO<sub>3</sub> substrate is confirmed, as is the quality nature of the interfaces therein. Further, the domain structure of the PMN-PT can be extracted by probing the projected lead-cation displacements, calculated as the shift of the lead-cation columns from the centroid of the nearest-neighbor magnesium/niobium/titaniumoxygen columns throughout the film (Figures 3B and 3C). These lead-cation displacements are mapped across an  $\sim 100 \times 100$  nm area of the film and reveal nanoscale regions having similar displacement directions and magnitude indicative of a nanoscale domain structure at zero voltage. An average domain size of ~7 nm (i.e., the length of the major axis of the ellipsoidal domains, Figure 3B) was extracted and is consistent with previous results from synchrotron-based diffuse-scattering measurements. 15 Furthermore, these nanoscale domains show a broad distribution of domain-wall angles peaking at  $\sim$ 54° and  $\sim$ 126° (Figure 3D). Here, the domainwall angle is defined as the maximum change in polarization angle between each domain-wall unit cell and its first nearest neighbor and is estimated following an established procedure. <sup>16</sup> The presence of nanoscale domains <sup>11,12,16</sup> may help explain the relatively slow timescale ( $\sim$ 0.1 ms) for the freeze-out of the  $M_A$ -to- $M_C$  phase transition observed in the X-ray diffraction results.

#### **Domain-switching behavior**

Having established both the timescale for the  $M_A$ -to- $M_C$  phase transition and the domain structure, we directly probed the effect of frequency on switching behavior in frequency- and temperature-dependent polarization hysteresis loops measured in a similar frequency range (Figure 4A). The room-temperature hysteresis loops show that the polarization is saturated and has the same value regardless of measurement frequency (Figure 4A). The coercive field (E<sub>c</sub>) and hysteresis loss (inset, Figure 4A) show a rapid increase above 10 kHz, which is similar to where the frequency-limited suppression of the  $M_A$ -to- $M_C$  transition was observed in the X-ray diffraction results (Figure 2). The magnitude of coercive field is considerably smaller than the electric field at which  $M_A$ -to- $M_C$  phase transition occurs. This indicates that initial increase in polarization occurs mostly by distortion via the R-to- $M_A$  transition, which can occur continuously by small distortion<sup>23</sup> and is therefore expected to be much easier to

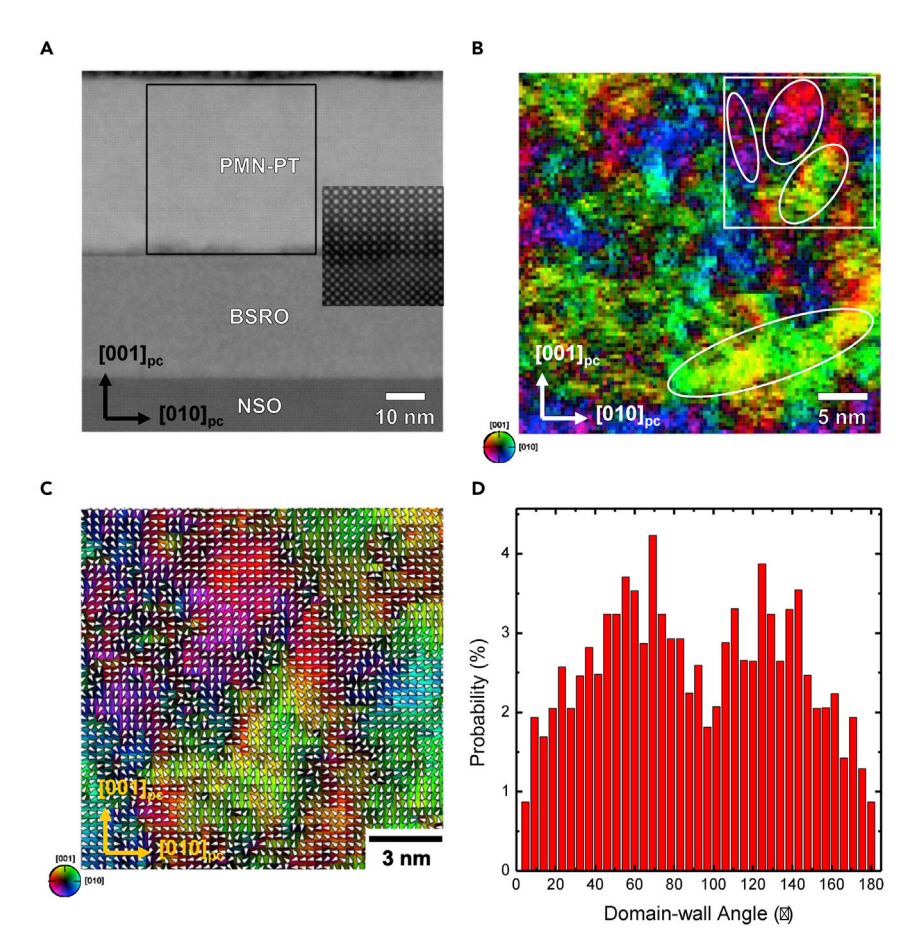


Figure 3. Atomic-resolution transmission electron microscopy studies

(A) HAADF STEM image of the full PMN-PT heterostructure wherein the inset shows a magnified HAADF image of the interface between the PMN-PT and the BSRO bottom electrode. NSO,  $NdScO_3$ .

- (B) Projected lead-cation displacement map calculated from the HAADF image, corresponding to the area in the black square in (A) The luminosity indicates the lead-cation displacement magnitudes (1–20 pm). Nanodomains with ellipsoidal shapes are marked by white lines.
- (C) Magnified region of the lead-cation displacement map, corresponding to the area in the white square in (B), showing changes in the lead-cation displacement direction locally.
- (D) Extracted domain-wall angle distribution as obtained from the lead-cation maps.

initiate than the  $M_A$ -to- $M_C$  phase transition. To examine switching dynamics, the activation field  $\alpha$ , which is the field required for nucleation and growth of antiparallel domains,  $^{24,25}$  was obtained using Merz's law,  $\tau \propto \frac{1}{t} \propto \exp^{\frac{\pi}{L_c}}$ , where  $\tau$  is the switching time and f is the measurement frequency.  $^{5,25}$   $\alpha$  can be determined from the magnitude of the slope in a plot of ln f versus  $1/E_c$ , here shown for temperatures from  $25^{\circ}C$  to  $125^{\circ}C$  (Figure 4B). Increasing the temperature above the  $M_A$ -to- $M_C$  phase transition temperature of  $\approx 80^{\circ}C^4$  allows for the examination of the effect of the ground state ( $M_A$  versus  $M_C$ ) on the switching dynamics. As expected,  $E_c$  ( $1/E_c$ ) decreases (increases) when f decreases or temperature increases. Notably, we see two linear regions, below and above 10 kHz, at temperatures from  $25^{\circ}C$  to  $75^{\circ}C$  (where the ground state is  $M_A$  with a small fraction of R), while only one linear region is observed at  $125^{\circ}C$  (where the ground state is expected to be  $M_C$ ). The values of  $\alpha$  were extracted by fitting these linear regions, which are labeled as  $\alpha_{low}$  and  $\alpha_{high}$  for frequencies below and above 10 kHz, respectively (inset, Figure 4B). At  $25^{\circ}C$ ,  $\alpha_{low}$  is



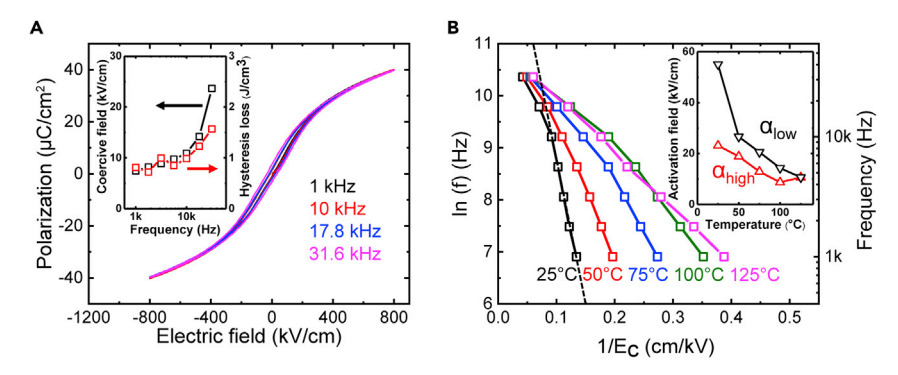


Figure 4. Frequency dependence of electrical properties

(A) Polarization-electric field hysteresis loops at various frequencies and room temperature. Inset: coercive field and hysteresis loss versus frequency.

(B) Frequency and temperature dependence of the coercive field. The dashed line shows an extrapolation of the low-frequency region to show the deviation at 10 kHz. Inset: activation field at low (black) and high (red) frequencies versus temperature.

much larger (55 kV/cm) than  $\alpha_{high}$  (23.1 kV/cm). From this observation, it can be hypothesized that the field-induced  $M_A$ -to- $M_C$  phase transition in the low-frequency region makes the activation of domain growth more difficult, which is likely due to the first-order nature of  $M_A$ -to- $M_C$  phase transition. This hypothesis can be tested by examining the temperature dependence of  $\alpha$ . Above the  $M_A$ -to- $M_C$  phase transition temperature, there should be only one  $\alpha$  due to the absence of a field-induced  $M_A$ -to- $M_C$  phase transition. As the temperature increases, both  $\alpha_{low}$  and  $\alpha_{high}$  become smaller and approach each other in magnitude, which supports this hypothesis.

#### **DISCUSSION**

Our combined results of in operando X-ray diffraction, STEM, and ferroelectric switching studies show the suppression of polarization rotation at ultrasonic frequencies (≥ 20 kHz), <sup>13</sup> which is hypothesized to be due to the existence of a high density of low-angle domain walls in relaxors. 5,12,15,16,26 Recent theoretical studies estimated that the domain-wall regions in PMN-PT can have an extremely high piezoelectric coefficient ( $d_{33} > 30,000 \, pC/N$ ) and thus may play a key role in ultrahigh piezoelectricity in relaxors.<sup>8</sup> The in operando X-ray diffraction results suggest that the mesoscale domain structures are strongly coupled to the average unit-cell structures and thus have dominant effects on the dynamics of polarization rotation. The STEM confirms the existence of a high density of low-angle domain walls in PMN-PT, which suggests that domain-wall motion may play a key role in determining the observed polarization-rotation dynamics. The reduction of  $\alpha$  above ultrasonic frequencies, which arises from suppression of the MA-to-MC phase transition, explains the observation of larger domain size upon AC-field poling. 10 Overall, our results suggest that suppression of the MA-to-MC phase transition at high frequency leads to the coarser domain structure observed in AC-field-poled PMN-PT, which has been linked to enhanced transparent optical characteristics. The observation of suppressed phase-transition behavior also clarifies the nature of suppressed polarization-saturation behavior, which is useful for designing relaxor-based capacitive dielectrics with high energy density.<sup>27</sup> This study, therefore, leads to a better understanding of the complex nature of the dynamics of relaxor ferroelectrics where multiscale structures are intricately related and compete against one another. Future studies investigating dynamic changes in the diffuse scattering under an AC electric





field, thus observing how domain walls respond to electric fields dynamically, would therefore be extremely valuable to understand the role of domain walls for ultrahigh piezoelectricity in relaxors.

#### **EXPERIMENTAL PROCEDURES**

#### Resource availability

#### Lead contact

Further information and requests for resources should be directed to and will be fulfilled by the lead contact, Lane W. Martin (lwmartin@berkeley.edu).

#### Materials availability

This study did not generate new unique reagents.

#### Data and code availability

All experimental data are available upon reasonable request to the lead contact.

#### Heterostructure growth

Heterostructures of 100 nm SRO/50 nm PMN-PT/25 nm BSRO were grown on NdScO $_3$  (110) single-crystal substrates (Crystec GmbH) from ceramic targets of the same chemistry via pulsed-laser deposition using a KrF excimer laser (248 nm, COMPex, Coherent) in an on-axis geometry. The BSRO layer, to be used as a bottom electrode for subsequent electrical studies, was grown at a heater temperature of 750°C in a dynamic oxygen pressure of 20 mtorr at a laser repetition rate of 3 Hz and a laser fluence of 1.85 J cm $^{-2}$ . The PMN-PT films were grown at a heater temperature of 600°C in a dynamic oxygen pressure of 200 mtorr at a laser repetition rate of 2 Hz and a laser fluence of 1.8 J cm $^{-2}$ . To enable subsequent electrical measurements, a 100 nm SRO layer was grown as a top electrode at a reduced temperature of 550°C to avoid the volatilization of lead in a dynamic oxygen pressure of 100 mtorr at a laser repetition rate of 15 Hz and a laser fluence of 1.33 J cm $^{-2}$ . Following growth, the heterostructures were cooled to room temperature at a rate of 5°C min $^{-1}$ , in a static oxygen pressure of 700 torr.

#### **Device fabrication**

A microfabrication process was used to produce devices that enable reliable electrical contact during in operando measurements of the PMN-PT thin films (Figure S1). The details of the process are as follows. First, the 100 nm SRO/50 nm PMN-PT/ 25 nm BSRO/NdScO<sub>3</sub> heterostructures were grown via pulsed-laser deposition. Second, the heterostructures were spin-coated with photoresist, which was subsequently defined to be bar shaped by photolithography. Third, the sample was ionmilled for a total depth of  $\sim$ 300 nm over 30 min ( $\sim$ 10 nm/min) at a beam voltage of 300 V, acceleration voltage of 45 V, and beam current of 5 mA to reach the substrate outside the photoresist. Fourth, the remaining photoresist was patterned into circular shapes with a diameter of 50 µm. Fifth, a second ion-milling step was performed for 14 min to define the circular SRO top electrodes and remove excess PMN-PT outside the circular region. Sixth, an MgO layer was grown at room temperature in a dynamic oxygen pressure of 20 mtorr at a laser repetition rate of 15 Hz and a laser fluence of 2 J cm<sup>-2</sup> to serve as an insulating layer. Seventh, the photoresist was removed with acetone to expose the SRO top electrode regions. Eighth, another lithography step was used to make inverse patterns of external platinum contact pads using photoresist. Then, 80 nm thick platinum was sputter deposited at room temperature and a target power of 100 W in a dynamic argon pressure of 2 mtorr. The photoresist was subsequently removed with acetone. Finally, the platinum contact pads were wire bonded to a chip carrier to apply an electric field along the [001].



#### Structural characterization

Laboratory-based X-ray diffraction  $\theta$ - $2\theta$  line scans and 2D reciprocal space-mapping studies were conducted at room temperature with a high-resolution X-ray diffractometer (X'pert Pro2, PANalytical). A wide-angle  $\theta$ - $2\theta$  line scan (Figure S16) shows that the heterostructures are single phase and highly crystalline with an out-of-plane lattice parameter of 4.05 Å. Two-dimensional reciprocal space mapping (Figure S16) shows that the PMN-PT films are coherently strained to the substrate and composed of R and M<sub>A</sub> phases, as evidenced by two sharp peaks with the same  $Q_x$  but different  $Q_y$  values for M<sub>A</sub> phase and a broad peak with intermediate  $Q_y$  value for the R phase.

#### **Electrical characterization**

Electrical measurements were performed on circular capacitor structures of 100 nm SRO/50 nm PMN-PT/25 nm BSRO heterostructures. Temperature-dependent polarization-electric field hysteresis loops were measured at frequencies from 0.1 to 100 kHz up to maximum electric fields of 800 kV/cm (corresponding to 4 V) from room temperature to 125°C using a Precision Multiferroic tester (Radiant Technologies). The maximum temperature was chosen to be above the  $M_A$ -to- $M_C$  phase transition temperature ( $\sim\!60^{\circ}$ C) of bulk PMN-PT.  $^4$ 

#### Scanning transmission electron microscopy

The PMN-PT heterostructures were prepared for cross-sectional electron microscopy using a gallium focused ion beam (Thermo Fisher Scientific Helios 660). STEM characterization was performed with a probe-corrected Thermo Fisher Scientific Titan G3 60–300 kV operated at 200 kV with a probe convergence semi-angle of 18 mrad. HAADF images were collected with a collection semi-angle of 63–200 mrad. Drift and scan distortion were corrected using the RevSTEM method. Atom column centers were extracted from the HAADF image using a custom Python-based atom column indexing method. Projected lead-cation displacements were calculated with respect to the nearest-neighbor magnesium/niobium/titanium sublattice sites. An iDPC image (Figure S17A) along with oxygen octahedral distortion analysis is provided to further probe the existence of rhombohedral-like features in PMN-PT films (Figure S17B). Details of this analysis are available in Kumar et al. 16.

#### Synchrotron-based in operando X-ray microdiffraction with AC electric field

Synchrotron-based in operando X-ray microdiffraction was conducted at room temperature using a Huber four-circle diffractometer and Pilatus 100K pixel detector with X-ray energy of 10 keV at beamline 6-ID-B at the Advanced Photon Source, Argonne National Laboratory. The samples were mounted on a chip carrier and wire bonded, and the leads on the chip carrier were soldered to the voltage source after the chip carrier was mounted on the sample stage of the diffractometer. For the microdiffraction, a 25 µm pinhole was used. The active device was aligned by mapping the surface of the sample in the platinum 111-diffraction condition (Figure S2). After alignment of the X-ray beam with the active device, the sample was aligned for the PMN-PT 003-diffraction condition. A triangular waveform was used to apply the AC voltage in the frequency range of 0.1–100 kHz. This waveform was matched with 64 bins to record accumulated intensities at each voltage (Figure S2). To protect the sample from electrical breakdown, the minimum frequency and maximum voltage were set to be 0.1 kHz and 4 V, respectively. To estimate the phase fraction as a function of voltage and frequency, the diffraction profile at each voltage was fitted using a Voigt function (0.1-25 kHz) (Figures S7-S14). The reciprocal lattice vector L was defined using the zero-field out-of-plane lattice parameter





of PMN-PT (4.05 Å) as 1 rlu  $\equiv$  1/4.05 Å. Empty squares in the figure represent data points for diffracted intensities. Orange lines represent the sum of the fitted curves. Individual fitting curves of red, green, and blue represent R, M<sub>A</sub>, and M<sub>C</sub> phases, respectively. Additional data for phase fraction (0.1–25 kHz) are provided (Figure S15). Raw data in the entire frequency range measured (0.1–100 kHz) are also provided (Figures S3–S6).

#### SUPPLEMENTAL INFORMATION

Supplemental information can be found online at https://doi.org/10.1016/j.matt. 2021.04.017.

#### **ACKNOWLEDGMENTS**

J.K. acknowledges support from the Intel FEINMAN program. A.K. and J.M.L. acknowledge support from the John Chipman Career Development Chair. A.F. acknowledges partial support from the National Science Foundation under grant OISE-154907 and from the NSF GRFP. G.A.P.V. acknowledges support from the National Science Foundation under grant DMR-1708615 and from the NSF GRFP. Z.T. acknowledges support from the Army Research Office under Grant W911NF-21-1-0126. L.W.M. acknowledges support from the Army Research Office under Grant W911NF-21-1-0118. This research used resources of the Advanced Photon Source, a US Department of Energy (DOE) Office of Science User Facility operated for the DOE Office of Science by Argonne National Laboratory under Contract No. DE-AC02-06CH11357.

#### **AUTHOR CONTRIBUTIONS**

Conceptualization, J.K. and D.M.; methodology, J.K., A.K., A.F., J.-W.K., and P.J.R.; software, D.M., A.K., J.-W.K., and P.J.R.; formal analysis, J.K. and D.M.; investigation, J.K., D.M., and P.J.R., resources, G.V. and Z.T.; writing – original draft, J.K.; writing – review & editing, J.K., A.K., A.F., J.M.L., P.J.R., and L.W.M.; visualization, J.K., D.M., and A.K.; supervision, P.J.R., J.M.L., and L.W.M.; funding acquisition, L.W.M.

#### **DECLARATION OF INTERESTS**

The authors declare no competing interests.

Received: March 8, 2021 Revised: April 13, 2021 Accepted: April 22, 2021 Published: May 18, 2021

#### **REFERENCES**

- 1. Cross, L.E. (1987). Relaxor ferroelectrics. Ferroelectrics 76, 241–267.
- Park, S.-E., and Shrout, T.R. (1997). Ultrahigh strain and piezoelectric behavior in relaxor based ferroelectric single crystals. J. Appl. Phys. 82, 1804–1811.
- 3. Fu, H., and Cohen, R.E. (2000). Polarization rotation mechanism for ultrahigh electromechanical response in single-crystal piezoelectrics. Nature 403, 281–283.
- 4. Bai, F., Wang, N., Li, J., Viehland, D., Gehring, P.M., Xu, G., and Shirane, G. (2004). X-ray and neutron diffraction investigations of the
- structural phase transformation sequence under electric field in 0.7Pb(Mg<sub>1/3</sub>Nb<sub>2/3</sub>)-0.3PbTiO<sub>3</sub> crystal. J. Appl. Phys. 96, 1620–1627.
- Fu, D., Taniguchi, H., Itoh, M., Koshihara, S., Yamamoto, N., and Mori, S. (2009).
   Relaxor Pb(Mg<sub>1/3</sub>Nb<sub>2/3</sub>)O<sub>3</sub>: a ferroelectric with multiple inhomogeneities. Phys. Rev. Lett. 103, 207601.
- Toulouse, J. (2008). The three characteristic temperatures of relaxor dynamics and their meaning. Ferroelectrics 369, 203–213.
- Li, F., Zhang, S., Yang, T., Xu, Z., Zhang, N., Liu, G., Wang, J., Wang, J., Cheng, Z., Ye, Z.-G.,

- et al. (2016). The origin of ultrahigh piezoelectricity in relaxor-ferroelectric solid solution crystals. Nat. Commun. 7, 13807.
- 8. Bell, A.J., Shepley, P.M., and Li, Y. (2020). Domain wall contributions to piezoelectricity in relaxor-lead titanate single crystals. Acta Mater. 195, 292–303.
- Xu, G., Zhong, Z., Bing, Y., Ye, Z.-G., and Shirane, G. (2006). Electric-field-induced redistribution of polar nano-regions in a relaxor ferroelectric. Nat. Mater. 5, 134–140.
- 10. Qiu, C., Wang, B., Zhang, N., Zhang, S., Liu, J., Walker, D., Wang, Y., Tian, H., Shrout, T.R., Xu,



- Z., et al. (2020). Transparent ferroelectric crystals with ultrahigh piezoelectricity. Nature 577, 350–354.
- Sato, Y., Hirayama, T., and Ikuhara, Y. (2011). Real-time direct observations of polarization reversal in a piezoelectric crystal: Pb(Mg<sub>1/3</sub>Nb<sub>2/3</sub>)O<sub>3</sub>-PbTiO<sub>3</sub> studied via in situ electrical biasing transmission electron microscopy. Phys. Rev. Lett. 107, 187601.
- Takenaka, H., Grinberg, I., Liu, S., and Rappe, A.M. (2017). Slush-like polar structures in single-crystal relaxors. Nature 546, 391–395.
- Kholkin, A., Tantigate, C., and Safari, A. (1998). Electromechanical properties of PMN-PT thin films prepared by pulsed laser deposition technique. Integr. Ferroelectr. 22, 515–523.
- 14. Little, E.A. (1955). Dynamic behavior of domain walls in barium titanate. Phys. Rev. 98, 978–984.
- Kim, J., Takenaka, H., Qi, Y., Damodaran, A.R., Fernandez, A., Gao, R., McCarter, M.R., Saremi, S., Chung, L., Rappe, A.M., et al. (2019). Epitaxial strain control of relaxor ferroelectric phase evolution. Adv. Mater. 31, 1901060.
- Kumar, A., Baker, J.N., Bowes, P.C., Cabral, M.J., Zhang, S., Dickey, E.C., Irving, D.L., and LeBeau, J.M. (2021). Atomic-resolution electron microscopy of nanoscale local structure in lead-based relaxor ferroelectrics. Nat. Mater. 20, 62–67.
- 17. Matsuura, M., Hirota, K., Gehring, P.M., Ye, Z.-G., Chen, W., and Shirane, G. (2006).

- Composition dependence of the diffuse scattering in the relaxor ferroelectric compound  $(1-x)Pb(Mg_{1/3}Nb_{2/3})O_3-xPbTiO_3$   $(0 \le x \le 0.40)$ . Phys. Rev. B 74, 144107.
- Seshadri, S.B., Prewitt, A.D., Studer, A.J., Damjanovic, D., and Jones, J.L. (2013). An in situ diffraction study of domain wall motion contributions to the frequency dispersion of the piezoelectric coefficient in lead zirconate titanate. Appl. Phys. Lett. 102, 042911.
- Vanderbilt, D., and Cohen, M.H. (2001). Monoclinic and triclinic phases in higherorder Devonshire theory. Phys. Rev. B 63, 094108.
- Chen, Z., Luo, Z., Huang, C., Qi, Y., Yang, P., You, L., Hu, C., Wu, T., Wang, J., Gao, C., et al (2011). Low-symmetry monoclinic phases and polarization rotation path mediated by epitaxial strain in multiferroic BiFeO3 thin films. Adv. Funct. Mater. 21, 133–138.
- 21. Kutnjak, Z., Petzelt, J., and Blinc, R. (2006). The giant electromechanical response in ferroelectric relaxors as a critical phenomenon. Nature 441, 956–959.
- Ohwada, K., Hirota, K., Rehrig, P.W., Gehring, P.M., Noheda, B., Fujii, Y., Park, S.-E.E., and Shirane, G. (2001). Neutron diffraction study of the irreversible R-M<sub>A</sub>-M<sub>C</sub> phase transition in single crystal Pb[(Zn<sub>1/3</sub>Nb<sub>2/3</sub>)<sub>1-x</sub>Ti<sub>x</sub>]O<sub>3</sub>. J. Phys. Soc. Jpn. 70, 2778–2783.

- Davis, M. (2007). Picturing the elephant: giant piezoelectric activity and the monoclinic phases of relaxor-ferroelectric single crystals. J. Electroceram. 19, 25–47.
- Merz, W.J. (1954). Domain formation and domain wall motions in ferroelectric BaTiO<sub>3</sub> single crystals. Phys. Rev. 95, 690–698.
- Wieder, H.H. (1957). Activation field and coercivity of ferroelectric barium titanate. J. Appl. Phys. 28, 367–369.
- Otoničar, M., Bradeško, A., Fulanović, L., Kos, T., Uršič, H., Benčan, A., Cabral, M.J., Henriques, A., Jones, J.L., Riemer, L., et al. (2020). Connecting the multiscale structure with macroscopic response of relaxor ferroelectrics. Adv. Funct. Mater. 2006823.
- Kim, J., Saremi, S., Acharya, M., Velarde, G., Parsonnet, E., Donahue, P., Qualls, A., Garcia, D., and Martin, L.W. (2020). Ultrahigh capacitive energy density in ion-bombarded relaxor ferroelectric films. Science 369, 81–84.
- Sang, X., and LeBeau, J.M. (2014). Revolving scanning transmission electron microscopy: correcting sample drift distortion without prior knowledge. Ultramicroscopy 138, 28–35.
- Sang, X., Oni, A.A., and LeBeau, J.M. (2014). Atom column indexing: atomic resolution image analysis through a matrix representation. Microsc. Microanal. 20, 1764– 1771.